Polyaramid based flexible antibacterial coatings fabricated using laser-induced carbonisation and copper electroplating

Emil R. Mamleyev[1], Fabian Falk[1], Peter G. Weidler[2], Stefan Heissler[2], Sagar Wadhwa[1], Omar Nassar[1], C.N. Shyam Kumar[3,4], Christian Kübel[3,4,5], Christof Wöll[2], Monsur Islam[1], Dario Mager[1], and Jan G. Korvink[1]

[1]*Institute of Microstructure Technology, Karlsruhe Institute of Technology, Hermann-von-Helmholtz-Platz 1, 76344 Eggenstein-Leopoldshafen, Germany*
[2]*Institute of Functional Interfaces, Karlsruhe Institute of Technology, Hermann-von-Helmholtz-Platz 1, 76344 Eggenstein-Leopoldshafen, Germany*
[3]*Institute of Nanotechnology, Karlsruhe Institute of Technology, Hermann-von-Helmholtz-Platz 1, 76344 Eggenstein-Leopoldshafen, Germany*
[4]*Department of Materials and Earth Sciences, Technical University Darmstadt, 64287 Darmstadt, Germany*
[5]*Karlsruhe Nano Micro Facility, Karlsruhe Institute of Technology, Hermann-von-Helmholtz-Platz 1, 76344 Eggenstein-Leopoldshafen, Germany*

Keywords — Polyaramid, Laser-induced carbonisation, Copper electroplating, Flexible circuits, Antibacterial coating

Abstract

A method for the fabrication of flexible electrical circuits on polyaramid substrates is presented, based on laser-induced carbonisation followed by copper electroplating. Locally carbonised flexible sheets of polyaramid (Nomex), by laser radiation, creates rough and highly porous microstructures that show a higher degree of graphitisation compared to thermally carbonised Nomex sheet. The found recipe for laser-induced carbonisation creates conductivities of up to $\sim$45 S cm^{-1}, thereby exceeding that observed for thermally pyrolysed materials ($\sim$38 S cm^{-1}) and laser carbon derived from Kapton using same laser wavelength ($\sim$35 S cm^{-1}). The electrical conductivity of the carbonised tracks was further improved by electroplating with copper. To demonstrate the electrical performance, fabricated circuits were tested and improvement of the sheet resistance was determined. Copper films exhibit antimicrobial activity and were used to fabricate customised flexible antibacterial coatings. The integration of laser carbonisation and electroplating technologies in a polyaramid substrate points to the development of customised circuit designs for smart textiles operating in high temperature environments.

1

1 Introduction

The field of flexible electronics has gained significant attention over the last decade, due to its great potential in many emerging applications, such as wearable electronics, smart textiles, health monitoring devices, portable energy storage devices, and radio frequency identification devices (RFID)[1, 2, 3, 4]. The benefits of flexible substrates allow applications in areas where the much faster and more efficient conventional electronics cannot be used. Laser-induced carbonisation (LIC) of flexible polymeric substrates has been recognised as one of the methods to fabricate conductive tracks with custom designs. In LIC, the polymer is selectively decomposed by a combination of photochemical and photothermal processes to a carbon-rich porous film [5, 6, 7]. Polyimide (commercially known as Kapton) has been extensively used by many researchers as polymer substrate for LIC, and has been demonstrated for different applications, including supercapacitors[8], adsorbents [9], catalysis platforms [10, 11], biosensors [12, 13], and mechanical and peizoresistive sensors [14, 15]. Additional polymers have been explored as suitable substrate for LIC. For example, Chyan et al. reported on the formation of laser carbon on a number of high-temperature thermoset materials, and on natural polymers such as lignin and cellulose [16]. LIC of high performance polymers such as polyaramid [16], polyetherimide (Ulse) [8], polysulfone, and polyphenylsulfone [17] have also been demonstrated. However, a more detailed investigation of the laser-induced carbonisation of some of these high performance polymers is still needed to expand the scope of LIC into new applications. An example of such a candidate polymer is polyaramid.

Polyaramids are a class of high performance polymeric fibre materials, which are broadly available as poly(p-phenylene tereph-talamide) (commercially known as Kevlar®) and poly(m-phenylene isophtalamide) (commercially known as Nomex®). These polyaramid fibres feature a high tensile strength (2900-3600 MPa), a high elastic modulus (70.5-112.4 GPa), good chemical inertness (degradation only in formic acid), and a high thermal resistance $(0.04\text{-}0.25\,\mathrm{W\,m^{-1}\,K^{-1}})$ [18]. Such properties enable the polyaramid fibres to be a suitable material for various applications including structural reinforcement, fire resistance, insulation for electrical equipment, and filtration, e.g. in exhaust systems [19, 20]. The polyaramid fibres have also been investigated as a precursor to activated carbon, due to their densely packed and organised filament orientation. Such activated carbon, derived from polyaramid fibres, has been demonstrated for adsorbents, catalysts, and molecular sieves [21, 22]. Apart from thermal pyrolysis, laser-induced carbonisation of polyaramids has been demonstrated [16, 23, 24], which opens many opportunities for fast, versatile, and selective fabrication of flexible carbon-based electrodes, customised electrical circuit design directly on polymer substrates, for textile integrated sensing electronics in high temperature operations, and specialised coatings.

Antibacterial coating are especially interesting considering that nosocomial infections are becoming a major threat in the medical environment due to cross contamination of surfaces and the increase of antimicrobial resistance in pathogens [25]. The reduction of contaminants is usually achieved by frequent cleaning including the use of surface disinfectants. However, the use of these disinfectants can breed microbes that have developed a resistance against the antimicrobial substance, and which can also be linked to antibiotic resistance, making the microbe less susceptible to both surface disinfectants and antibiotics [26]. Once this resistance has manifested, the microbe can cover the environment, since it is not eliminated by

the cleaning procedure anymore. In the worst case this resistance can transfer to other microbes by horizontal gene transfer [27]. Antibacterial coatings based on copper and silver circumvent these resistances, and therefore are viable options to counteract microbial contamination and nosocomial infections [25, 28]. However, the majority of available coatings use bulk material dispersed in the matrix, which can be significantly reduced by targeted electroplating on the conductive surface.

In this work, we present a comparative analysis of copper electroplating on a laser carbon and a thermally pyrolysed precursor. Directly LIC processed polyaramid was fabricated as a demonstration of a targeted surface, and used as an antimicrobial coating, based on the potent activity of copper. To achieve this, we first perform a selective carbonisation of a flexible polyaramid insulation sheet using laser radiation, and then characterise the material properties of the resulting carbon tracks by using Raman spectroscopy, X-ray diffraction (XRD), Transmission electron microscopy (TEM) and energy-dispersive X-ray spectroscopy (EDX). We discuss the influence of the polymer processing settings on the quality of the resulting laser carbon, and demonstrate the influence of the different electrodes on the electrochemical deposition (electroplating) of copper. In general, the laser carbonised structures show an increased electrical conductivity, which makes it a preferable seed layer for electroplating. Such laser patterning followed by electroplating can be a direct route for a mask-free electrical design on the surface of a polymer. The kinetics of the electroplating were analysed using cyclic voltammetry (CV). Such customisation of a polyaramid substrates can also be a step towards the development of antibacterial coatings for large and small areas, fire resistant sensors and smart textiles.

2 Materials and Methods

2.1 Laser-induced carbonisation of Nomex

Poly(1,3-phenylene isophthalamide), commercially known as Nomex®Type 410 insulation paper (DuPont™; supplied by RS Components), of thickness 130 ± 13 µm, was rinsed with isopropanol and dried for 10 min naturally. The films were fixed on a glass slide with acrylic adhesive films (3M-467MP), to prevent film from warping during fabrication. Laser-induced carbonisation was carried out on a CO_2-laser (ULS Versa Laser 3.50, wavelength: 10.6 µm, lens 2.0', beam diameter 120 µm at focus). A single irradiation process exhibited deterioration of resistivity after fixing for electroplating, thus two different recipes with multiple irradiations were chosen for the manufacturing of laser carbon. The first type of laser carbon was fabricated with double irradiation. During a first scan, parameters were set to 3 W, $13 \, cm \, s^{-1}$ scanning speed, a focal distance of 2.5 mm, interline distance of $\sim$100 µm, a distance between pulses in a line at $\sim$65 µm, and during a second scan, the scanning speed was increased to $32 \, cm \, s^{-1}$ and the distance between pulses reduced to $\sim$25 µm. The sample is further referred to as LC2. The fabrication was repeated under nitrogen flow. The details are presented in the supplementary information. The second type was fabricated with a triple irradiation procedure, the first irradiation performed at 3 W, $13 \, cm \, s^{-1}$ scanning speed, a focal distance of 2.5 mm, an interline distance of $\sim$25 µm, and a distance between pulses in a line at $\sim$25 µm. The following procedures were repeated as for LC2, but the pulse distance was kept at $\sim$25 µm for all repetitions. This sample is further denoted as LC3.

For a comparison of material properties, we also prepared a sample by conventional thermal pyrolysis of Nomex paper. A heat treat-

ment recipe, widely used for the fabrication of carbon micro-electromechanical systems (C-MEMS) for conversion of the polymers into carbon [29, 30, 31], was used. The heat treatment was carried at 900 °C under nitrogen flow ($\sim$0.8 l/ min) for 1 h with a heating rate of 5 °C min^{-1}. The sample is further referred as N900.

2.2 Electroplating of copper

The electrode exposed to the electroplating electrolyte solution had a square shape with 10 mm side length as depicted in Figure 1.

Copper electroplating on LC2 and LC3 was conducted in a self-built electrolyte bath (Cuprostar LP-1, Enthone-OMIGmbH) with 2 M concentration of Cu_2SO_4, 7×10^{-4} M of H_2SO_4, 9×10^{-6} M of HCl following the manufacturer's specification for promoter additives. The bath was constantly stirred by an electric pump. A direct current was applied during plating in the 10-50 mA range using a home-built power source [32]. The deposition time was kept at 300 s for all specimens. The best plating regime was determined at 30 mA, where the sample showed retention of the resistance after bending and remained fixed to the substrate without damage. After electroplating, the samples were washed with de-ionised water and kept on a hotplate at 95 °C for 300 s for evaporation of the residual moisture, and prevention of copper oxidation. The thickness of the plated material can be estimated by the Faraday equation: $t = I\tau A/(nF\rho S)$, where t is the plated thickness, I the applied current, τ the plating time (300 s for all cases), A the atomic weight of the material ($A_{Cu} = 63.55$ g mol^{-1}), n the number of electrons transferred by the ion into the solution (n = 2), F Faraday's constant ($F = 96\,485$ s A mol^{-1}), ρ the material density ($\rho_{Cu} = 8.96$ g/cm^3), and S the electrode surface area. Due to the high porosity of the carbon material, the deposition spontaneously occurs within the whole electrode volume, so that the quantitative data on the specific surface area must be determined from gas adsorption (BET).

2.3 Material characterisation

A Bruker Vertex 70 spectrometer with ATR-FTIR was used for the determination of the absorbance in the 300-4000 cm^{-1} range, with 2 cm^{-1} resolution. The absorbance was corrected with a Kubelka-Munk function [33].

The surface morphology was studied with a Carl Zeiss AG - SUPRA 60VP SEM equipped with a Bruker X-FLASH 5010 energy-dispersive X-ray spectroscopy (EDX) detector. The laser carbon specimens remaining on the precursor substrate were grounded with copper tape on the edges in order to avoid charging, free standing specimens were fixed with carbon adhesive pad and did not display any charging. The EDX was utilised for the estimation of the elemental composition, and to perform an element sensitive mapping. For laser carbon samples, the thickness was measured with a Dektak V 220-Si profilometer by averaging both the step height of the carbonised area and the precursor height under the removed carbon film.

The specific surface area and porosity was determined from argon adsorption isotherms performed at 87 K with a Quantachrome Autosorb-1 MP via BET theory [34].

A Hioki 3540 mΩ HiTester was employed for the determination of sheet resistance, using a 4-probe van der Pauw geometry.

The elemental (combustion) analysis measurements were performed on a ELEMENTAR Vario Micro and determines the average value throughout thickness of the film. As analytical scale the model SARTORIUS M2P was used. The machine calibrated for determination of mass percent for hydrogen, carbon and nitro-

gen. A mass percent of oxygen was estimated by subtraction of determined elements, due to insignificant contribution of other elements in the precursor preparation and processing.

XRD was conducted on a Bruker D8 Advance diffractometer in a $\theta - \theta$ geometry using Cu-K$\alpha_{1,2}$ radiation. All carbon samples were studied in powder, LC3 was additionally studied in a film. All samples after copper electroplating were studied in a film. Bragg's formula was used for the determination of the interplane distance, and the Scherrer formula was used for the determination of crystallite size: $\tau = K\lambda/(\beta cos\theta)$, where τ is the mean size of the ordered crystallite, K is the shape factor, λ is the x-ray wavelength ($\lambda = 1.54\,\text{Å}$), β is the full width at half maximum (FWHM) of the selected reflection, and θ is Bragg's angle. The method described by Warren [35] was used to determine the crystallite size (L_a) and stacking thickness (L_c) in carbon, the K- shape factor specified at 1.84 and 0.89 respectively.

Raman spectroscopy was performed on a Bruker Senterra equipped with a DPSS laser ($\lambda = 532\,\text{nm}$) at $2\,\text{mW}$ power with a penetration depth of $< 1\,\mu\text{m}$ and measured in a spectral bandwidth of 70 - $3500\,\text{cm}^{-1}$ with $0.5\,\text{cm}^{-1}$ resolution.

Cyclic voltammetry was performed on a modular AutoLab PGSTAT128N potentiostat/galvanostat equipped with NOVA software. The measurements were carried out in a three-electrode system: a selected carbon working electrode, a platinum electrode, and a Ag / AgCl reference electrode was immersed in 1M HCl solution. All experiments were conducted under constant stirring conditions at 500 rpm. The applied potential was ranged between $-1\,\text{V}$ and $0.3\,\text{V}$, the sweep rates were $0.05\,\text{V\,s}^{-1}$, $0.1\,\text{V\,s}^{-1}$, $0.2\,\text{V\,s}^{-1}$, $0.5\,\text{V\,s}^{-1}$ and $1.0\,\text{V\,s}^{-1}$. The observation of the saturation current was performed in the range between $-8\,\text{V}$ and $0.3\,\text{V}$ under a $0.5\,\text{V\,s}^{-1}$ sweep rate. The copper electroplating kinetics were studied in the same electrolyte solution as electroplating as it was mentioned above. The rate of deposition was estimated by taking the derivative of the CV. The data from N900 and LC3 were processed without smoothing the curve, but in case LC2 the derivation was followed by smoothing using a Savitzky–Golay filter.

2.4 Evaluation of bactericidal activity

Due to exhibited flexibility of the composite film, the electroplated LC2 films (at $30\,\text{mA/cm}^2$) have been selected as carriers for the evaluation of antibacterial activity. Circular stainless steel carriers as well as square Nomex®410 insulation paper in standard and laser carbon forms were chosen as control carriers. *Escherichia coli* strain K12 grown in LB-Miller and *Bacillus subtilis* strain subsp. spizizenii grown in Mueller-Hinton-Broth, which are the respective model organisms for gram-negative and positive bacteria, were selected for the evaluation. Tests were done in triplicates according to a simplified EPA Copper surface test protocol to adjust to laboratory capacity and equipment. Both strains were restored from $-80\,°\text{C}$ Glycerol cryogenic stocks to nutrient plates. Overnight cultures were picked from the agar plates and grown for $18\,\text{h}$ in a glass beaker agitated by 120 rpm at $30\,°\text{C}$ for *Bacillus subtilis* and $37\,°\text{C}$ for *Escherichia coli*. As a working solution for the test bacteria, the overnight cultures were diluted to an optical density OD^{600} of 0.05 in culture media, supplemented with a soil load of $3\,\text{mg\,ml}^{-1}$ sterilised organic soil. All test carriers were exposed to UV-C light for $30\,\text{min}$ for sterilisation and subsequently inserted into a 24-well standard BRANDplate®. Following this step every carrier was submerged with $600\,\mu\text{l}$ bacterial working solution and dried for $75\,\text{min}$. Start of the test was initiated by washing and resuspending bacterial mass on the carriers

with PBS (0.01 mol, pH 7.4) for three consecutive times and processing the extracted mass by Miles and Misra method [36]. Dilutions of down to 1×10^{-7} were tested on nutrient plates. Each plate was divided into 4 segments and 50 µl total volume of each dilution was applied to each segment and incubated at optimal temperature for 18 h. The colonies counted from this initial resuspension will be regarded as initial microbial concentration at "zero elapsed time". After initiation the carriers were then incubated in static at for 2 h at 30 °C for *Bacillus subtilis* and 37 °C for *Escherichia coli*. Followed by incubation the carriers are transferred to an unused slot of the BRANDplate® and processed by Miles and Misra method [36] with the same conditions as in the initial process, subsequently incubated for 18 h at 30 °C for *Bacillus subtilis* and 37 °C for *Escherichia coli*. After incubation, the colonies on each plate were counted for each segment in a range of 30 to 300 colonies by hand. Everything above this range is regarded as too many to count, and everything below this range is regarded as too few to count and set to 0.

3 Results and Discussion

3.1 Optimization of laser carbonization

The polyaramid was selected for laser-induced carbonisation, due to its favourable properties for the formation of laser carbons, such as high thermal insulation, medium-range order, and high dissociation energy of single monomers [8, 16, 23]. In the selected IR region, the delivered energy is in the range of ~ 0.12 eV, and thus not sufficient for direct monomer dissociation. However, the applied radiation induces phonon vibrations in the affected region (943.4 cm^{-1}), responsible for out-of-plane bending of C$-$H bonds at the aromatic ring, which consequently dissipates along the molecular chains. The detailed FTIR absorbance spectrum is presented in Figure S1, and agrees with previous reports [37]. Due to the low thermal conductivity $(0.25$ W m^{-1} K$^{-1})$, the induced energy remains localised and causes a temperature increase, which results in bond dissociation [38, 39]. The laser-induced carbonisation happens over a threshold laser intensity of 2×10^4 W/cm^2. At the same time, a strongly ionised plume is observed above the surface, which is attributed to the expulsion of dissociated molecules under high pressure (~ 3 GPa) [39]. This plume causes partial shielding and further absorbs the laser radiation, which can substantially contribute to the temperature accumulation above the film. This phenomenon can lead to the surface temperature rising to over 2000 °C [40]. At such high temperatures, C$-$N and C$=$O bonds in the aramid chain rapture rapidly, corrupting the structural integrity of the chain and causing intensive expulsion of a number of species with complex aromatic structure [41, 42]. The precursor undergoes rapid graphitisation in combination with some of the ionised radicals and aromatic units recombining in stacks of misaligned graphene sheets, featuring surface functionality with a number of nitrogen and oxygen heteroatoms.

The focused laser beam resulted in the ablation of a significant part of the graphitised fragments, thus defocusing was introduced, resulting in an improvement of the carbon film, in terms of resistance, mechanical stability and in adhesion to the precursor substrate [43, 16]. On the other hand, this causes an increase in the minimal feature size for a single track to ~ 300 µm, but provides sufficient heating, initiating the LIC. Molecular dynamic simulations showed that the ablation is caused by an excessive temperature gradient, leading to the induction of high internal stresses causing cleavage of the carbonised fragments [44].
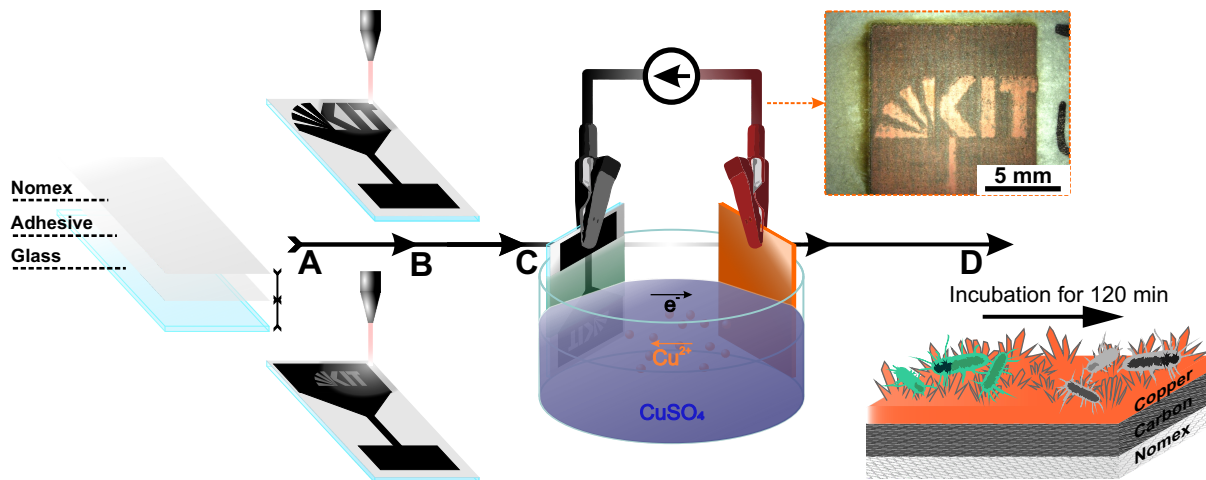
The fabrication scheme is presented in Fig-

Figure 1: Schematic representation of the fabrication process: (A) Nomex paper bonding to a glass slide. (B) Laser irradiation using LC2 and LC3 recipes. (C) Copper electroplating. (D) Antibacterial surface tests.

ure 1; briefly, the Nomex insulation paper was fixed on a glass slide with acrylic adhesive film, the precursor film was processed into laser carbon by CO_2 mid-IR laser radiation, followed by electroplating with copper. The new composite film was tested for the antibacterial properties.

The laser carbon fabricated with a single irradiation displayed significant deterioration of conductivity during preparation for electroplating, and a selected procedure exhibited non-uniform interface and fracture at the Nomex / laser carbon boundary. Nevertheless, it helped to establish suitable fabrication protocol and determine the operation parameters. For all further cases, the power and the working distance were kept at 3 W and 2.5 mm (Figure S2), but the quality was improved by introducing multiple passes over same area during fabrication.

In the first case, the laser irradiation was performed twice: during the initial irradiation, the distance between the pulses in one line was increased to 65 µm, providing initiation of the seed layer and improving optical

absorbance of the surface to a selected laser wavelength. According to the manufacturer, a decreased pulse throughput (increased pulse distance) delivers higher intensity pulses and keeps the average distributed intensity across the line at a selected value, which results in a larger heat affected zone. Then the second irradiation was performed with a standard pulse throughput, and with increased transition speed set to $32\,\mathrm{cm\,s^{-1}}$. Here, the first irradiation process with reduced pulse throughput provided precursor carbonisation into the seed layer, with increase of specific heat and optical absorbance, and the second irradiation induced annealing of the film with improving graphitisation. As previously stated by Chyan et al. [16], the double irradiation procedure can be performed at same laser parameters. However, we found the aforementioned procedure better suited to the processing of Nomex, more reproducible, and therefore useful for further fabrication.

In the second procedure, the parameters were kept the same as for a single irradiation, except for the interline distance, which

7

was decreased to $25\,\mu m$, and which provided pulse overlap around 90%. Typically in polyimides, such a close distance between rasterization lines leads to cleavage of the laser carbon and is found to be unfruitful [12]. However, the widening of the laser heat affected zone with reduced temperature gradient caused the formation of carbon with sufficient adhesion to the substrate. The second and third irradiation provided further annealing of the carbonised substrate. These samples could easily be released from the precursor film and studied on their own. Notably, during the final laser pass, the expulsion of a plume had been significantly reduced compared to previous steps, which was caused by reduction of released oxygen from the polymer, and affected only by oxygen from the processing interface.

3.2 Material and microstructural characterization of Nomex derived laser carbon

Figure 2 shows variations in surface morphology depending on the selected fabrication procedure. Figure 2A and B present morphology of a thermally carbonised calendar rolled Nomex film, which exhibited fibrous microstructure similar to the morphology of the precursor Nomex film. LC2 displays a significant porosity, ranging from hundreds of nanometer voids and wrinkles, to pores of over $10\,\mu m$ diameter (Figure 2C and D). Processing in nitrogen working environment featured close porous microstructure, but promoted formation of more rough surface (Figure S3). Figure 2E and F show the morphology of the sample LC3, which is substantially different from LC2, and features a reduced number of pores larger than $\sim 1\,\mu m$ in size, and an increase in the number of smaller pores of $\sim 100\,nm$ or less. The reduced interline distance between tracks induces higher localised temperature, which promotes better graphitisation and im-

proves absorbance coefficient over precursor's. This causes increase in temperature accumulation during repetition of the laser passing, which results in partial ablation in the interface carbon layers, exposing deeper microstructure with characteristic lower pore distribution [12]. Notably, the specific surface area, examined with gas sorption, confirms reduction LC3 in bulk, as well (Table 1). The thickness of the carbonised area in the laser carbons was measured to be $28.9 \pm 4.9\,\mu m$ and $25.3 \pm 2.7\,\mu m$ for LC2 and LC3. The electrical conductivity was measured to be $5.38 \pm 0.85\,S\,cm^{-1}$ and $45.22 \pm 10.68\,S\,cm^{-1}$ for LC2 and LC3 (Table 1).

Chemical analysis from the extracted powders is presented in Table 1. The sample N900 features the lowest carbon content at 77.27 ± 0.07 wt.% and the highest quantity from other elements among other samples. This fact indirectly confirms lower processing temperature comparatively to the LIC from Nomex. Notably, despite higher throughput during fabrication and higher conductivity of LC3, it features substantially lower quantity of carbon, with increased contribution from other heteroatoms in the lattice in comparison to LC2. Regardless of the lower degree of carbonisation, the conductivity is influenced by crystallinity and the pore distribution.

Figure 3A shows a powder X-ray diffractogram, where several prominent peaks are observed, characteristic for carbon-based materials. N900, LC2, and LC3 showed strong reflections at 24.3°, 25.8° and 25.8° respectively, which corresponds to a (002) plane suggesting the presence of stacking of graphite basal planes [45, 46, 47, 48]. The peak observed at at $\sim 44.4°$ for N900 indicates amorphous carbon. Other prominent peaks were detected 43.0° and 43.1° for LC2 and LC3 respectively, which can be assigned to reflections by the (100) graphite plane. The interline distances and crystallite sizes were determined from the peaks, which
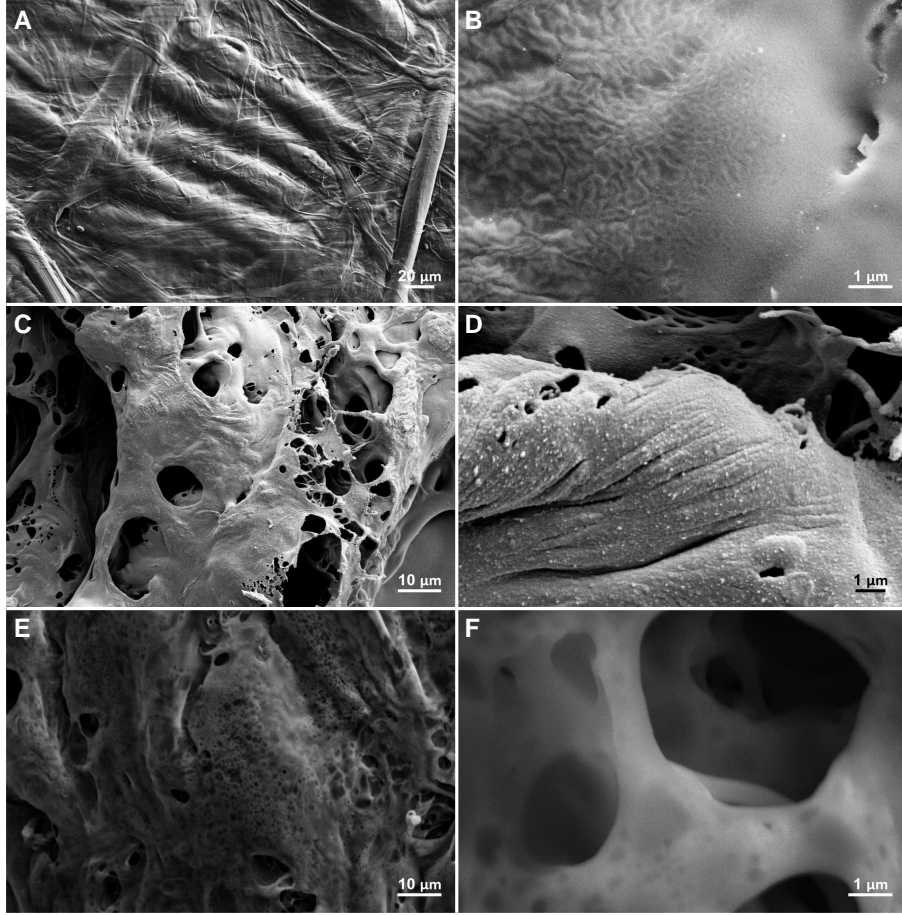
Figure 2: Scanning electron microscopy of the surface morphology: (A - B) thermally pyrolysed Nomex (N900), after laser-induced carbonisation (C - D) LC2 and (E - F) LC3.

Table 1: Properties of pyrolysed Nomex and laser carbons LC2 and LC3.

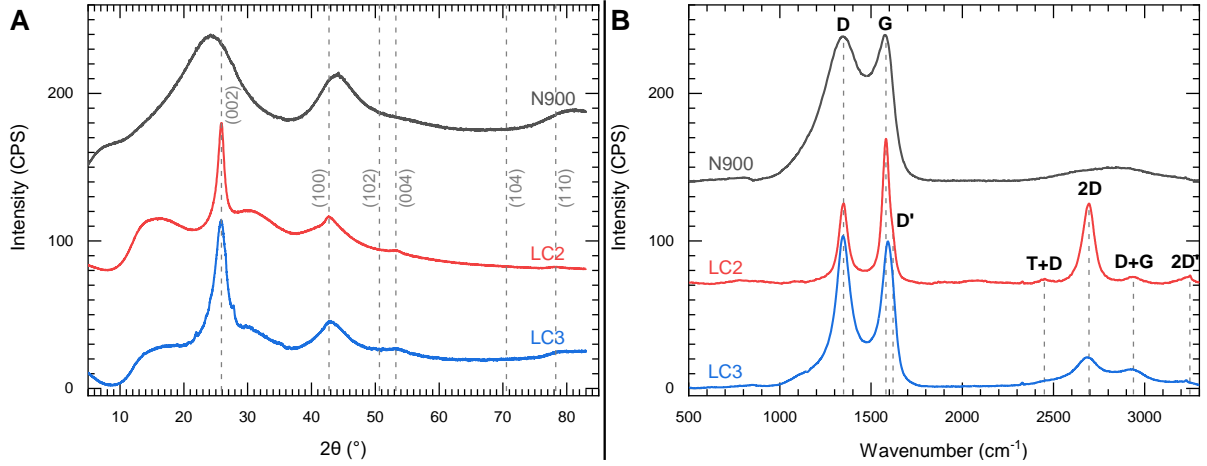|		N900	LC2	LC3
Specific surface area (BET), m^2/g			117	71
Conductivity, S/cm^2		37.9 ± 11.4	5.44 ± 1.07	45.22 ± 10.68
Elemental analysis, wt.%	C	77.27 ± 0.07	97.25 ± 0.40	90.24 ± 0.06
	H	1.31 ± 0.02	0.30 ± 0.03	0.39 ± 0.04
	N	7.35 ± 0.04	0.94 ± 0.06	1.77 ± 0.06
	O	14.07	1.52	7.60
Crystallite size (L$_a$), nm		2.0	3.8	4.3
Stacking thickness (L$_c$), nm		1.0	7.0	5.6
Interlayer distance, Å		3.69	3.45	3.45

9

Figure 3: (A) X-ray diffractogram of N900, LC2 and LC3. (B) Raman spectra measured from N900, LC2 and LC3.

were fit with a Lorentzian (Table 1). Other peaks representative of the graphitic carbons could be indexed according space-group #173 $P6_3$, and the strong reflections were observed only in the laser carbons at $\sim53°$ and $\sim78°$ corresponding to the (004) and (110) planes. Laser carbon fabricated in nitrogen did not indicate any additional features in the diffractogram (Figure S4). The XRD of the powder extracted from both laser carbons exhibit similar features. However, LC3 measured as a film (Figure S5), exhibited splitting into two peaks at 42.9° and 46.4°, the latter could be indexed for the rhombohedral graphite phase at $(110)_R$ plane according to space-group $R\bar{3}m$ [49, 50] with crystallite size along the plane calculated at 10 nm.

The interlayer distance was determined using Bragg's law[51], and showed significant differences between pyrolysed and laser carbons. N900 showed a d-spacing of 3.69 Å, whereas the d-spacing of both LC2 and LC3 were 3.45 Å (Table 1). The XRD analysis further confirmed the improvement of graphitisation in the laser carbon samples in comparison to N900, featuring an increase in crystalline size

(L_a) and stacking thickness (L_c), with reduced interlayer distances. It is known that polymer derived carbons exhibit in-plane defects with variation of the valence angles between basal planes, which causes broadening of the reflections compared to the commercially available graphite [52, 47].

Raman spectroscopy is shown in Figure 3B, which confirms polymer conversion to carbon through the prominent peaks observed at $\sim1345\,\mathrm{cm}^{-1}$, $\sim1580\,\mathrm{cm}^{-1}$ and $\sim2690\,\mathrm{cm}^{-1}$, assigned to the D, G and 2D bands. The D-band arise from an A_{1g} breathing mode of the hexagonal rings at the K-point initiated by disorder, the G-band from an E_{2g} mode at the Γ-point, responsible for the stretching vibrations in carbon. The 2D-band arise from a second-order overtone originating from sp^2 carbons [53]. LC2 exhibited some additional prominent peaks detected at $\sim1620\,\mathrm{cm}^{-1}$, $\sim2450\,\mathrm{cm}^{-1}$, $\sim2935\,\mathrm{cm}^{-1}$ and $\sim3250\,\mathrm{cm}^{-1}$ corresponding to the D', T+D, D+G and 2D' bands [54]. All laser carbons exhibit higher I_G/I_D ratios than thermally pyrolysed carbon (Table 2), which suggests a higher degree of graphitisation, confirming and

Table 2: Peak position, FWHM of Raman bands and calculated areal band ratio (I_G/I_D) and hybridisation ratio (I_{2D}/I_G).

	D-band		G-band		2D-band		I_G/I_D	I_{2D}/I_G
	Position, cm^{-1}	FWHM, cm^{-1}	Position, cm^{-1}	FWHM, cm^{-1}	Position, cm^{-1}	FWHM, cm^{-1}		
N900	1343	261.5	1575	90.8	-	-	0.28	-
LC2	1348	57.5	1582	48.4	2692	69.6	1.55	0.55
LC3	1348	111.3	1590	74.9	2681	162.6	0.68	0.21

indicating substantial increase in the sp^2 hybridised state by the I_{2D}/I_G ratio. LC3 exhibited an increase in FWHM for all observed bands, and in the intensity of the D-band, suggesting a reduction of ordering in the lattice. Moreover, it featured intensity reduction and a shift of 2D overtone to 2681 cm^{-1}, and an increased D+G combinational peak at 2929 cm^{-1}, which can be attributed to an increase in contribution of the first-order D-band to the spectrum.

The nature of laser-induced carbonisation is significantly different from conventional furnace-based pyrolysis, where gas expulsion induces high pressures with extreme temperature gradients during polycondensation, resulting in wrapping graphene sheets, internal stresses, and fragmentation with variable crystallite sizes [39]. This was further confirmed with TEM imaging (Figure S6 and Figure S7), that featured the presence of carbon with short range of periodicity in N900. However, the laser carbon showed the presence of long, crumbled and thin crystallites, which were attributed to features of glassy carbon [55]. Overall, LC2 features higher degree of graphitisation, determined from Raman peak ratio I_G/I_D, and increased quantity of sp^2-hybridised carbon with thinner graphene stacks determined from I_{2D}/I_G (Table 2). The XRD confirmed this assumption, supported by the bigger crystallite size observed for both laser carbons. However, the film of LC3 exhibited a reduction of the crystallite size in the hexagonal phase, but presence of the rhombohedral phase with significant increase in the crystallite size along $(110)_R$ plane. Typically, the rhombohedral phase of graphite emanates from unidirectional shear stress in a hexagonal lattice [56], which is inherited due to the kinetics of LIC. Notably, the mismatch of carbon atoms between A-B-C graphene stacks and the reduction of carbon content observed with elemental analysis result in a widening of 2D, D+G Raman bands, suggested by DFT calculations and experimental studies [57, 58]. The rhombohedral phase suggests the occurrence of a dispersionless electronic band at the Fermi level with a bandwidth smaller than 2 meV [59], thus providing improvement in conductivity [58]. These features are in agreement with the observed characteristics of fabricated LC3 film, but were not observed in powder XRD. Due to the metastable nature of this carbon allotrope, the transition to the hexagonal phase was found after annealing at 1300 °C for 1 hour under an argon environment [56]. A significant drop in conductivity was observed to (20.34 ± 4.92) S cm^{-1} for the thermally annealed LC3 sample. The XRD performed on the annealed LC3 exhibited a crystallite size reduction at $(110)_R$ plane to 9.76 nm and increase in the hexagonal $(100)_H$ plane to 3.62 nm (Figure S5, Table S2), which could be attributed to a short duration of the process and annealing only at the phase transition boundary temperature. Further detailed investigation on the nature of formation and evolution of the rhombohedral phase is required, and is not within the scope of the cur-

rent manuscript.

3.3 Copper electroplating on laser carbon

The Cu electroplating is a redox reaction where the oxidation takes place at the anode with simultaneous reduction of the cathode, which leads to the deposition of a Cu layer on the target material. To overcome the potential difference of the reaction, an external current is provided. The kinetics of electroplating were studied with cyclic voltammetry (CV), which is depicted in Figure 4. A peak was observed at $0.1\,\mathrm{V}$ only for N900, and can be attributed to a reduction on the site of the oxygen heteroatom (Figure 4A). The peak area was reduced with increase in scanning speed, which suggests depletion of the electron transfer equilibrium on the surface [60]. All samples displayed two plating regimes: a steady state deposition, without any significant peaks attributed to reduction/oxidation, and a saturation current regime. For all samples, the steady-state regime switched at $\sim -60\,\mathrm{mA/cm^2}$. Indeed, during electroplating, the deposition was limited and showed current overflow after increase above the saturation current, which corresponds to limitation of Cu^{2+} ion flow due to a hydrogen evolution reaction on the electrode surface [60]. The threshold voltage was dependent on the resistance of the selected specimen, and observed at $\sim -0.3\,\mathrm{V}$, $\sim -1.7\,\mathrm{V}$ and $\sim -0.4\,\mathrm{V}$ for N900, LC2 and LC3 respectively. As observed in Figure 4A, C, and E, the number of cycles performed did not have any significant contribution to the plating behaviour. However, the saturation current increased with the number of cycles (insets of Figure 4A, C, and E), suggesting an improvement in conductivity by plating. The derivative of the current was taken to determine the highest electroplating rate, which showed increase after each cycle. However, the rate, characteristic to

plating on selected specimen, retained within small deviation, thus the mean deposition rate was estimated after averaging and listed in Table 3. The data indicated that the highest rate of electroplating was achieved for N900, which can be attributed to the lower sample resistance, smaller specific surface area and better charge distribution in the surface of the sample. A significantly lower deposition rate was observed for LC2, which corresponds to the largest specific surface area (Table 1). Nevertheless, LC3 resulted in comparable deposition rate and threshold voltage. Considering the ease of fabrication through laser irradiation, the sample LC3 can be a suitable alternative to the furnace carbonised sample N900.

Figure 5A shows a reduction of the sheet resistance with an increase of the applied current density in a semi-log plot, recorded after a plating duration of $300\,\mathrm{s}$. Notably, a film with electroplated copper on LC3 exhibited a significantly lower sheet resistance, following a higher deposition rate as discussed above, and reaching a minimum at $(6.63 \pm 0.86) \times 10^{-2}\,\Omega\,\mathrm{sq^{-1}}$. The limiting current density was observed for LC2 at $40\,\mathrm{mA/cm^2}$, above which an overpotential was observed and plating became constrained. The samples, electroplated at $30\,\mathrm{mA/cm^2}$, were selected for further studies due to their retention of adhesion, flexibility and resistance properties under bending. The LC3 exhibited highest mass increase after plating (Table 3), but the film was constrained in bending. LC3 specimen showed exfoliation of the carbon/copper film from the Nomex substrate during bending test. Therefore, it was performed only for the selected LC2, which showed good flexibility at $90°$ bending radius without any exfoliation and insignificant degradation of the surface. After 500 cycles, the sheet resistance dropped to $30\,\%$, which shows good retention of conductivity (Figure S8). The films showed degradation overtime, by oxidation to Cu_xO, which was es-

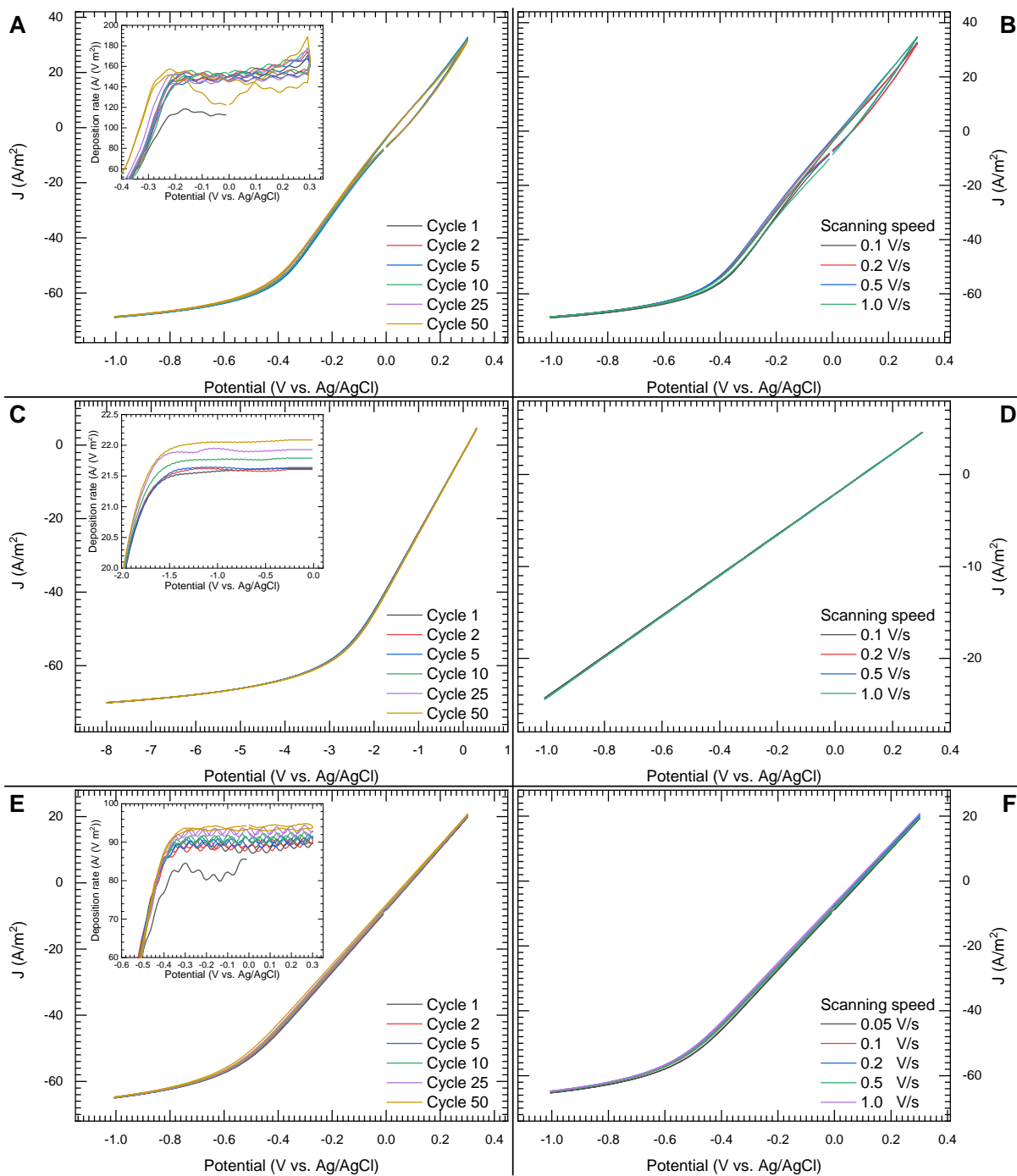Figure 4: Cyclic voltammetry for the deposition of copper performed in 2 M Cu$_2$SO$_4$ solution on (A-B) N900, (C-D) LC2 and (E-F) LC3. (A, C, E) performed at $0.1\,\mathrm{V\,s^{-1}}$ after selected cycles. (B, D, F) 5th cycle at selected scanning speed.
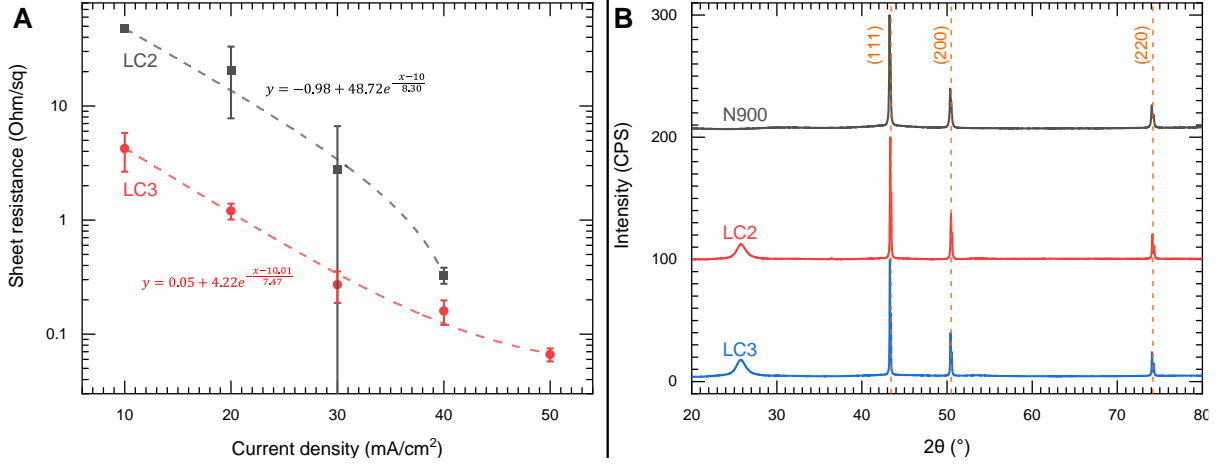
Figure 5: (A) Variation of the sheet resistance with current density. Electroplating was performed for 300 s in all cases. (B) X-ray diffraction of electroplated films.

Table 3: The electroplating rate and crystallographic properties of plated copper.

		N900	LC2	LC3
Deposition rate, $V/(Am^2)$		139.3 ± 13.3	21.8 ± 0.2	91.0 ± 1.8
Mass of deposited copper, mg		10 ± 5	14 ± 4	42 ± 17
(111)	Peak position, °	43.24	43.32	43.28
	d, Å	2.09	2.09	2.09
	L, nm	80.00	98.10	122.30
(200)	Peak position, °	50.37	50.45	50.41
	d, Å	1.81	1.81	1.81
	L, nm	58.33	81.90	103.40
(220)	Peak position, °	74.05	74.12	74.08
	d, Å	1.29	1.28	1.28
	L, nm	66.71	95.40	116.50

timated by EDX and sheet resistance increase (Figure S9). The oxidation saturated after a week of storage and showed resistance increase in 10 % and 30 % for LC2 and LC3 respectively.

The XRD performed for this composite film (Figure 5B) showed strong reflections at 25.9°, 43.3°, 50.4° and 74.1°; the first peak corresponds to the carbon (002) plane, the remain-

ing peaks are contributed by the (111), (200) and (220) reflections of copper respectively. The positions of these peaks correspond to the $Fm\overline{3}m$ space-group. The splitting of the peaks was observed in all copper reflections, due to a doublet in the radiation source. The peaks were fitted with a Lorentzian and the crystallite sizes were determined using the Scherrer formula, listed in Table 3. The copper crystal-

14

lite size increased with improvement of graphitisation, featuring the smallest size deposited on N900, and the largest for LC3. The structure inheritance from carbon film facilitated copper growth in substantially more organised fashion for LC3, resulting in the largest crystallites, and due to a low ordering present in N900, the crystallites were grown the smallest [61].

Figure 6A-F shows the surface morphology of the composite after discrete current electroplating on N900, LC2 and LC3. In each case, the copper deposited as an elongated crystal with length over 3.8 ± 1.3 µm, 3.2 ± 0.9 µm and 3.0 ± 1.3 µm, and width 1.1 ± 0.5 µm, 1.1 ± 0.3 µm and 1.1 ± 0.5 µm for N900, LC2 and LC3 respectively. In LC3, the distribution in length of the crystals was observed over a wider range. All crystals were fixed on a central active site, and continuously interconnected with neighbouring crystals, providing electrical stability. The electroplated film contained areal coverage with copper of 81.72 %, 36.22 % and 20.28 % for N900, LC2 and LC3 determined from SEM imaging. The grown film thickness was determined as 3.7 µm using Faraday's equation implementing only surface area $1\,cm^2$. However, the average thickness of the electroplated copper exceeded calculated value, due to preference in the deposition sites.

3.4 Plated copper for antibacterial activity

Table 4 shows a reduction in the quantity of the bacterial colonies upon initial exposition to the LC2 copper carriers of *E. coli* and *B. subtilis*. Copper ions generating from the copper surface can generate reactive oxygen species in a Fenton-like reaction, which can cause damage to lipids, protein and DNA [62]. Furthermore, copper destabilises iron-sulphur clusters, which are required in the active center and as

co-factors in many vital enzymes, ultimately leading to the death of the cell [62]. In general gram-positive bacteria are less susceptible to copper exposure, especially so if they are from the class of micrococci [63]. The initial exposure time of the 75 minute drying process, before the first samples for the Miles and Misra method are extracted. However, it was sufficient to eliminate any measurable trace of the species *E. coli* and *B. subtilis*, which explains why the data after incubation is unavailable for both. In the case of the LC2 carrier, the amount of colony forming units extracted after first exposure is drastically increased for *B. subtilis* and decreased for *E. coli*. The results for *B. subtilis* suggest that in comparison to steel it is more difficult for the Bacilli to attach to the carbon surface. *E. coli* bacteria are struggling to increase their biomass on this carrier during incubation time, while the amount of *B. subtilis* is significantly decreased. It is known, that the nanostructures inhibit or even eliminate bacterial growth [64, 65]. While both LC2 and the copper plated LC2 carriers have nanocrystalline features, that can potentially hinder bacterial growth. However, the bactericidal effect of the LC2 copper carrier originates from the decisive lethality of copper ions. Nomex paper itself is able to decrease the amount of bacteria extracted after initial exposure, but both bacteria were able to significantly increase their biomass after an incubation after 2 h, so while it prevents bacterial adhesion it does not hinder their growth significantly.

The large discrepancy between the colony counts, after incubation of the two organisms, can be explained by the different growth rates and surface adhesion properties of the species. While *E. coli* K12 has a doubling time of approximately 15 -20 min [66] and very poor adhesion characteristics on steel surfaces [67], *B. subtilis* species has a doubling time of approximately 120 min [68], and is a model organism
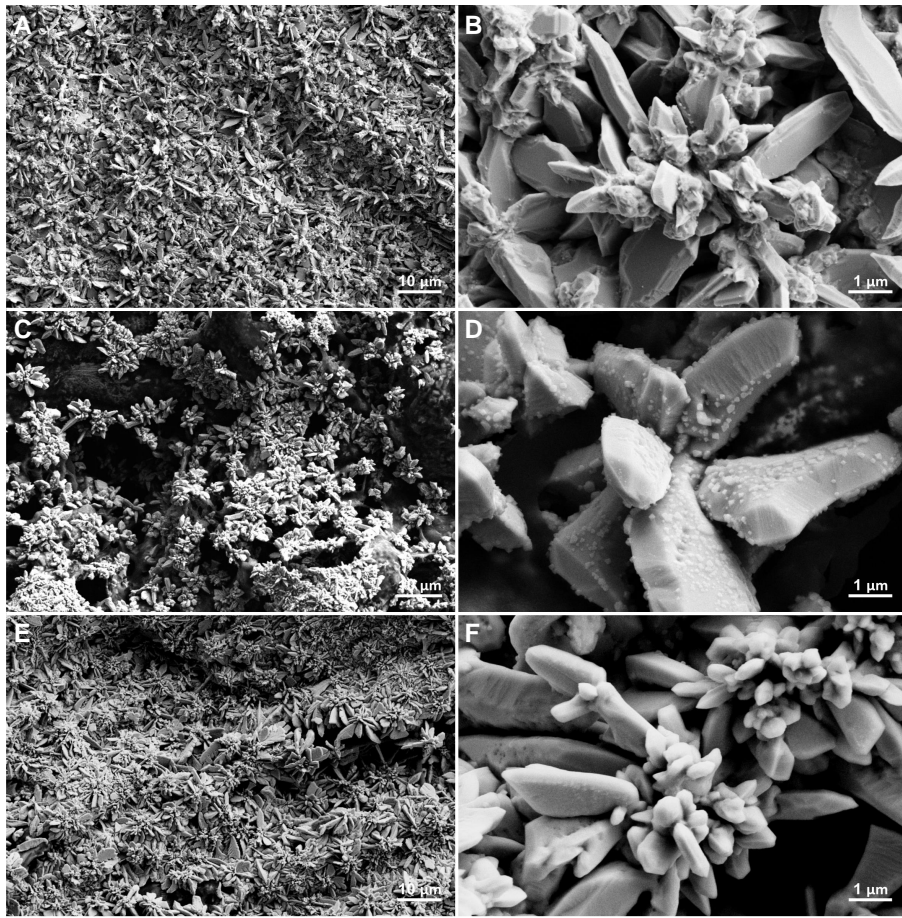
Figure 6: Surface morphology after electroplating: (A-B) N900, (C-D) LC2 and (E-F) LC3.

Table 4: Percentage of bacterial count based on the amount of colony forming units after initial exposition (i.E.) in comparison to the initial colony amount counted on steel control carriers and after incubation (a.I.) in comparison to the initial amount counted on the individual carriers.

Carrier	E. coli i.E.	E. coli a.I.	B. subtilis i.E.	B. subtilis a.I.
Stainless steel		677 %		19 %
Nomex paper	3 %	894 %	3 %	219 %
LC2	40 %	133 %	271 %	4 %
LC2 Copper	>0.1 %	N/A	>0.1 %	N/A

for adhesion and biofilm formation [69]. In comparison to *B. subtilis*, *E. coli* is able to increase its biomass faster and more of it is flushed from the carrier during sample extraction.

The results show that the copper electroplated on the carbon film antimicrobial activities are similar to other antimicrobial copper

16

surfaces [70]. Combined with the properties ease of fabrication [8, 16] and controllable copper plating thickness as well as flexibility of the material, this enables access to a reliable and cost-efficient antimicrobial surface.

We observed that the PBS (0.01 mol, pH 7.4) acquired a blue taint during the resuspension steps of the LC2 copper carriers. This taint is characteristic to presence of the copper ions in the solution, confined in coordination complexes as $CuCl_2, Cu_3(PO_4)_2, Cu(HPO_4)_2$ and $CuSO_4$ originating from PBS and residual electrolyte. However, only a minor contribution of sulphur was detected by EDX analysis after drying the assay on a reference gold-coated silicon chip, with elemental composition predominately originating from Na, Cl, P, characteristic for the content of PBS (Table S5; mapping in Figure S11). Therefore, it was concluded that only copper ions were effectively involved in the antimicrobial properties. However, the quantitative determination of the copper ions with titration did not provide any sufficient results, due to strong dilution during procedure (Figure S13), and near neutral pH, which constrains use of the colour indicators. For qualitative evaluation, the FTIR was performed for assays before and after incubation, and characteristic vibrational modes of H_{20} and some ions from PBS were observed.

4   Conclusion

We have demonstrated the selective carbonisation of tracks embedded in a Nomex precursor substrate. The technique is versatile and allows for the fabrication of carbon into arbitrary planar shapes. The two most promising recipes were determined and studied. One of the recipes exhibited a metastable rhombohedral phase, which was observed for the first time in such systems, and exhibited one of the highest electrical conductivities for laser carbons fabricated in the selected laser wavelength ($35 \, \mathrm{S \, cm^{-1}}$) and the highest for polyaramides. To further improve the electrical conductivity and thereby increase the applicability of the approach, electroplating of copper in the volume of the carbon film was also investigated, and the kinetics discussed. The quantity of deposited copper could be controlled, and thereby could be adjusted depending on application requirements. As a demonstration, the LC2 copper film and its precursor were tested as an antibacterial coating. While the copper film itself showed the elimination of countable colonies after the initial exposition of *E. coli* and *B. subtilis*, its carbon precursor significantly decreased the growth rate of *E. coli* and overall amount of colonies of *B. subtilis* significantly. The porosity and surface activity, in conjunction with thin copper layers, is suitable for use as disposable antimicrobial surface, but also for flexible sensing electronics, molecular sieves, catalysis, and could also potentially serve as a hydrogen storage platform.

17

Acknowledgements

Completing Interests

The authors declare no conflict of interest.

Supporting Information

Details on a material selection, comparison between different preparation procedures, including characterisation with Raman spectroscopy, XRD, TEM. For the selected materials provided details deterioration of the conductive properties after a bending test, an oxidation over time, a copper deposition rate. After exposure of the film to bacteria provided details on the extended analysis of the colony forming unit, and study on the resulting by-product with EDX and titration.

References

[1] M. Stoppa and A. Chiolerio, "Wearable electronics and smart textiles: a critical review," *sensors*, vol. 14, no. 7, pp. 11957–11992, 2014.

[2] G. Schwartz, B. C.-K. Tee, J. Mei, A. L. Appleton, D. H. Kim, H. Wang, and Z. Bao, "Flexible polymer transistors with high pressure sensitivity for application in electronic skin and health monitoring," *Nature communications*, vol. 4, p. 1859, 2013.

[3] X. Wang, X. Lu, B. Liu, D. Chen, Y. Tong, and G. Shen, "Flexible energy-storage devices: design consideration and recent progress," *Advanced materials*, vol. 26, no. 28, pp. 4763–4782, 2014.

[4] R. Singh, E. Singh, and H. S. Nalwa, "Inkjet printed nanomaterial based flexible radio frequency identification (rfid) tag sensors for the internet of nano things," *RSC Advances*, vol. 7, no. 77, pp. 48597–48630, 2017.

[5] R. Srinivasan, B. Braren, and R. W. Dreyfus, "Ultraviolet laser ablation of polyimide films," *Journal of Applied Physics*, vol. 61, pp. 372–376, jan 1987.

[6] R. Srinivasan, "Ablation of polyimide (Kapton™) films by pulsed (ns) ultraviolet and infrared (9.17 μm) lasers," *Applied Physics A Solids and Surfaces*, vol. 56, pp. 417–423, may 1993.

[7] R. Srinivasan, R. R. Hall, W. D. Wilson, W. D. Loehle, and D. C. Allbee, "Formation of a Porous, Patternable, Electrically Conducting Carbon Network by the Ultraviolet Laser Irradiation of the Polyimide PMDA-ODA (Kapton)," *Chemistry of Materials*, vol. 6, pp. 888–889, jul 1994.

[8] J. Lin, Z. Peng, Y. Liu, F. Ruiz-Zepeda, R. Ye, E. L. G. Samuel, M. J. Yacaman, B. I. Yakobson, and J. M. Tour, "Laser-induced porous graphene films from commercial polymers," *Nature Communications*, vol. 5, p. 5714, 2014.

[9] K. Rathinam, S. P. Singh, Y. Li, R. Kasher, J. M. Tour, and C. J. Arnusch, "Polyimide derived laser-induced graphene as adsorbent for cationic and anionic dyes," *Carbon*, vol. 124, no. 2, pp. 515–524, 2017.

[10] F. Clerici, M. Fontana, S. Bianco, M. Serrapede, F. Perrucci, S. Ferrero, E. Tresso, and A. Lamberti, "In situ MoS 2 Decoration of Laser-Induced Graphene as Flexible Supercapacitor Electrodes," *ACS Applied Materials & Interfaces*, vol. 8, pp. 10459–10465, apr 2016.

[11] J. Zhang, M. Ren, L. Wang, Y. Li, B. I. Yakobson, and J. M. Tour, "Oxidized Laser-Induced Graphene for Efficient Oxygen Electrocatalysis," *Advanced Materials*, vol. 30, no. 21, pp. 1–7, 2018.

[12] E. R. Mamleyev, S. Heissler, A. Nefedov, P. G. Weidler, N. Nordin, V. V. Kudryashov, K. Länge, N. MacKinnon, and S. Sharma, "Laser-induced hierarchical carbon patterns on polyimide substrates for flexible urea sensors," *npj Flexible Electronics*, vol. 3, p. 2, dec 2019.

[13] X. Xuan, J. Y. Kim, X. Hui, P. S. Das, H. S. Yoon, and J.-Y. Park, "A highly stretchable and conductive 3d porous graphene metal nanocomposite based electrochemical-physiological hybrid biosensor," *Biosensors and Bioelectronics*, vol. 120, pp. 160–167, 2018.

[14] L. Q. Tao, H. Tian, Y. Liu, Z. Y. Ju, Y. Pang, Y. Q. Chen, D. Y. Wang, X. G. Tian, J. C. Yan, N. Q. Deng, Y. Yang, and T. L. Ren, "An intelligent artificial throat with sound-sensing ability based on laser induced graphene," *Nature Communications*, vol. 8, pp. 1–8, 2017.

[15] X. Duan, J. Luo, Y. Yao, and T. Liu, "A Route toward Ultrasensitive Layered Carbon Based Piezoresistive Sensors through Hierarchical Contact Design," *ACS Applied Materials & Interfaces*, vol. 9, pp. 43133–43142, dec 2017.

[16] Y. Chyan, R. Ye, Y. Li, S. P. Singh, C. J. Arnusch, and J. M. Tour, "Laser-Induced Graphene by Multiple Lasing: Toward Electronics on Cloth, Paper, and Food," *ACS Nano*, vol. 12, no. 3, pp. 2176–2183, 2018.

[17] S. P. Singh, Y. Li, J. Zhang, J. M. Tour, and C. J. Arnusch, "Sulfur-Doped Laser-Induced Porous Graphene Derived from Polysulfone-Class Polymers and Membranes," *ACS Nano*, vol. 12, pp. 289–297, jan 2018.

[18] R. Young, D. Lu, R. Day, W. Knoff, and H. Davis, "Relationship between structure and mechanical properties for aramid fibres," *Journal of materials science*, vol. 27, no. 20, pp. 5431–5440, 1992.

[19] D. A. Holmes, "Textiles for survival," *Handbook of technical textiles*, vol. 12, p. 461, 2000.

[20] F. Xiao and X. Liu, "Design improvement on diesel particulate bag filters," tech. rep., SAE Technical Paper, 1994.

[21] M. Blanco López, A. Martınez-Alonso, and J. Tascón, "N2 and CO2 adsorption on activated carbon fibres prepared from Nomex chars," *Carbon*, vol. 38, no. 8, pp. 1177–1182, 2000.

[22] S. Villar-Rodil, R. Denoyel, J. Rouquerol, A. Martınez-Alonso, and J. Tascón, "Porous texture evolution in nomex-derived activated carbon fibers," *Journal of colloid and interface science*, vol. 252, no. 1, pp. 169–176, 2002.

[23] F. Al-Sulaiman, B. S. Yilbas, F. C. Karakas, M. Ahsan, and E. M. A. Mokheimer, "Laser hole cutting in Kevlar: Modeling and quality assessment," *International Journal of Advanced Manufacturing Technology*, vol. 38, no. 11-12, pp. 1125–1136, 2008.

[24] F. Al-Sulaiman, B. S. Yilbas, M. Ahsan, and C. Karatas, "CO2 laser cutting of Kevlar laminate: influence of assisting gas pressure," *The International Journal of Advanced Manufacturing Technology*, vol. 45, pp. 62–70, nov 2009.

[25] D. A. Montero, C. Arellano, M. Pardo, R. Vera, R. Gálvez, M. Cifuentes, M. A. Berasain, M. Gómez, C. Ramírez, and R. M. Vidal, "Antimicrobial properties of a novel copper-based composite coating with potential for use in healthcare facilities," *Antimicrobial Resistance & Infection Control*, vol. 8, no. 1, pp. 1–10, 2019.

[26] D. E. Carey and P. J. McNamara, "The impact of triclosan on the spread of antibiotic resistance in the environment," *Frontiers in microbiology*, vol. 5, p. 780, 2015.

[27] N. A. Lerminiaux and A. D. Cameron, "Horizontal transfer of antibiotic resistance genes in clinical environments," *Canadian journal of microbiology*, vol. 65, no. 1, pp. 34–44, 2019.

[28] M. Raffi, S. Mehrwan, T. M. Bhatti, J. I. Akhter, A. Hameed, W. Yawar, and M. M. Ul Hasan, "Investigations into the antibacterial behavior of copper nanoparticles against Escherichia coli," *Annals of Microbiology*, vol. 60, no. 1, pp. 75–80, 2010.

[29] R. Natu, M. Islam, J. Gilmore, and R. Martinez-Duarte, "Shrinkage of su-8 microstructures during carbonization," *Journal of Analytical and Applied Pyrolysis*, vol. 131, pp. 17–27, 2018.

[30] C. S. Sharma, A. Sharma, and M. Madou, "Multiscale carbon structures fabricated by direct micropatterning of electrospun mats of su-8 photoresist nanofibers," *Langmuir*, vol. 26, no. 4, pp. 2218–2222, 2010.

[31] M. Islam, J. Flach, and R. Martinez-Duarte, "Carbon origami: A method to fabricate lightweight carbon cellular materials," *Carbon*, vol. 133, pp. 140–149, 2018.

[32] O. Nassar, M. V. Meissner, S. Wadhwa, J. G. Korvink, and D. Mager, "Load sensitive stable current source for complex

precision pulsed electroplating," *Review of Scientific Instruments*, vol. 90, no. 10, p. 104704, 2019.

[33] P. Kubelka, "Ein beitrag zur optik der farbanstriche (contribution to the optic of paint)," *Zeitschrift fur technische Physik*, vol. 12, pp. 593–601, 1931.

[34] S. Brunauer, P. H. Emmett, and E. Teller, "Adsorption of gases in multimolecular layers," *Journal of the American chemical society*, vol. 60, no. 2, pp. 309–319, 1938.

[35] B. E. Warren, "X-ray diffraction in random layer lattices," *Physical Review*, vol. 59, no. 9, pp. 693–698, 1941.

[36] A. A. Miles, S. Misra, and J. Irwin, "The estimation of the bactericidal power of the blood," *Epidemiology & Infection*, vol. 38, no. 6, pp. 732–749, 1938.

[37] S. Villar-Rodil, A. Martınez-Alonso, and J. M. D. Tascón, "Studies on pyrolysis of Nomex polyaramid fibers," *Journal of Analytical and Applied Pyrolysis*, vol. 58-59, pp. 105–115, apr 2001.

[38] Y. Wang, Y. Wang, P. Zhang, F. Liu, and S. Luo, "Laser-Induced Freestanding Graphene Papers: A New Route of Scalable Fabrication with Tunable Morphologies and Properties for Multifunctional Devices and Structures," *Small*, vol. 14, no. 36, pp. 1–9, 2018.

[39] Y. Dong, S. C. Rismiller, and J. Lin, "Molecular dynamic simulation of layered graphene clusters formation from polyimides under extreme conditions," *Carbon*, vol. 104, pp. 47–55, 2016.

[40] X. Ruan, R. Wang, J. Luo, Y. Yao, and T. Liu, "Experimental and modeling study of CO2 laser writing induced polyimide carbonization process," *Materials & Design*, vol. 160, pp. 1168–1177, dec 2018.

[41] J. H. Brannon, J. R. Lankard, A. I. Baise, F. Burns, and J. Kaufman, "Excimer laser etching of polyimide," *Journal of Applied Physics*, vol. 58, pp. 2036–2043, sep 1985.

[42] D. J. Doyle and J. M. Kokosa, "The laser cutting of kevlar: A study of the chemical by-products," *Materials and Manufacturing Processes*, vol. 5, no. 4, pp. 609–615, 1990.

[43] A. F. Carvalho, A. J. S. Fernandes, C. Leitão, J. Deuermeier, A. C. Marques, R. Martins, E. Fortunato, and F. M. Costa, "Laser-Induced Graphene Strain Sensors Produced by Ultraviolet Irradiation of Polyimide," *Advanced Functional Materials*, vol. 28, no. 52, pp. 1–8, 2018.

[44] Y. Chen, J. Long, S. Zhou, D. Shi, Y. Huang, X. Chen, J. Gao, N. Zhao, and C. Wong, "UV Laser-Induced Polyimide-to-Graphene Conversion: Modeling, Fabrication, and Application," *Small Methods*, vol. 3, p. 1900208, oct 2019.

[45] J. Biscoe and B. E. Warren, "An X-Ray Study of Carbon Black," *Journal of Applied Physics*, vol. 13, pp. 364–371, jun 1942.

[46] J. Y. Howe, C. J. Rawn, L. E. Jones, and H. Ow, "Improved crystallographic data for graphite," *Powder Diffraction*, vol. 18, pp. 150–154, jun 2003.

[47] Z. Li, C. Lu, Z. Xia, Y. Zhou, and Z. Luo, "X-ray diffraction patterns of graphite and turbostratic carbon," *Carbon*, vol. 45, no. 8, pp. 1686–1695, 2007.

[48] B. Manoj and A. Kunjomana, "Study of stacking structure of amorphous carbon

by x-ray diffraction technique," *Int. J. Electrochem. Sci*, vol. 7, no. 4, pp. 3127–3134, 2012.

[49] J. C. Arrebola, A. Caballero, L. Hernan, and J. Morales, "Graphitized Carbons of Variable Morphology and Crystallinity: A Comparative Study of Their Performance in Lithium Cells," *Journal of The Electrochemical Society*, vol. 156, no. 12, p. A986, 2009.

[50] D. Aurbach, H. Teller, and E. Levi, "Morphology/Behavior Relationship in Reversible Electrochemical Lithium Insertion into Graphitic Materials," *Journal of The Electrochemical Society*, vol. 149, no. 10, p. A1255, 2002.

[51] W. H. Bragg and W. L. Bragg, "The reflection of x-rays by crystals," *Proceedings of the Royal Society of London. Series A, Containing Papers of a Mathematical and Physical Character*, vol. 88, no. 605, pp. 428–438, 1913.

[52] F. Tuinstra and J. L. Koenig, "Raman spectrum of graphite," *The Journal of Chemical Physics*, vol. 53, no. 3, pp. 1126–1130, 1970.

[53] A. C. Ferrari and D. M. Basko, "Raman spectroscopy as a versatile tool for studying the properties of graphene," *Nature nanotechnology*, vol. 8, no. 4, p. 235, 2013.

[54] S. Bukalov, L. Leites, A. Sorokin, A. Kotosonov, *et al.*, "Structural changes in industrial glassy carbon as a function of heat treatment temperature according to raman spectroscopy and x-ray diffraction data," *: , , ,* vol. 5, no. 1, 2014.

[55] S. Sharma, C. S. Kumar, J. G. Korvink, and C. Kübel, "Evolution of glassy carbon microstructure: in situ transmission electron microscopy of the pyrolysis process,"

Scientific reports, vol. 8, no. 1, p. 16282, 2018.

[56] F. Laves and Y. Baskin, "On the Formation of the Rhombohedral Graphite Modification," *Zeitschrift fur Kristallographie - New Crystal Structures*, vol. 107, no. 5-6, pp. 337–356, 1956.

[57] A. Torche, F. Mauri, J. C. Charlier, and M. Calandra, "First-principles determination of the Raman fingerprint of rhombohedral graphite," *Physical Review Materials*, vol. 1, no. 4, pp. 1–5, 2017.

[58] H. Henck, J. Avila, Z. Ben Aziza, D. Pierucci, J. Baima, B. Pamuk, J. Chaste, D. Utt, M. Bartos, K. Nogajewski, B. A. Piot, M. Orlita, M. Potemski, M. Calandra, M. C. Asensio, F. Mauri, C. Faugeras, and A. Ouerghi, "Flat electronic bands in long sequences of rhombohedral-stacked graphene," *Physical Review B*, vol. 97, no. 24, pp. 1–6, 2018.

[59] R. Xiao, F. Tasnádi, K. Koepernik, J. W. Venderbos, M. Richter, and M. Taut, "Density functional investigation of rhombohedral stacks of graphene: Topological surface states, nonlinear dielectric response, and bulk limit," *Physical Review B - Condensed Matter and Materials Physics*, vol. 84, no. 16, pp. 1–15, 2011.

[60] E. Gyenge, J. Jung, and B. Mahato, "Electroplated reticulated vitreous carbon current collectors for lead-acid batteries: Opportunities and challenges," *Journal of Power Sources*, vol. 113, no. 2, pp. 388–395, 2003.

[61] J. Czochralski, "Ein neues Verfahren zur Messung der Kristallisationsgeschwindigkeit der Metalle," *Zeitschrift*

für Physikalische Chemie, vol. 92U, pp. 219–221, jan 1918.

[62] C. L. Dupont, G. Grass, and C. Rensing, "Copper toxicity and the origin of bacterial resistance—new insights and applications," *Metallomics*, vol. 3, no. 11, pp. 1109–1118, 2011.

[63] C. E. Santo, P. V. Morais, and G. Grass, "Isolation and characterization of bacteria resistant to metallic copper surfaces," *Applied and environmental microbiology*, vol. 76, no. 5, pp. 1341–1348, 2010.

[64] P. Doll, A. Al-Ahmad, A. Bacher, A. Muslija, R. Thelen, L. Hahn, R. Ahrens, B. Spindler, and A. Guber, "Fabrication of silicon nanopillar arrays by electron beam lithography and reactive ion etching for advanced bacterial adhesion studies," *Materials Research Express*, vol. 6, no. 6, p. 065402, 2019.

[65] A. Tripathy, P. Sen, B. Su, and W. H. Briscoe, "Natural and bioinspired nanostructured bactericidal surfaces," *Advances in colloid and interface science*, vol. 248, pp. 85–104, 2017.

[66] A. G. Marr, "Growth rate of escherichia coli.," *Microbiology and Molecular Biology Reviews*, vol. 55, no. 2, pp. 316–333, 1991.

[67] C. Beloin, A. Roux, and J.-M. Ghigo, "Escherichia coli biofilms," in *Bacterial biofilms*, pp. 249–289, Springer, 2008.

[68] I. Burdett, T. Kirkwood, and J. Whalley, "Growth kinetics of individual bacillus subtilis cells and correlation with nucleoid extension.," *Journal of bacteriology*, vol. 167, no. 1, pp. 219–230, 1986.

[69] H. Vlamakis, Y. Chai, P. Beauregard, R. Losick, and R. Kolter, "Sticking together: building a biofilm the bacillus sub-

tilis way," *Nature Reviews Microbiology*, vol. 11, no. 3, pp. 157–168, 2013.

[70] G. Grass, C. Rensing, and M. Solioz, "Metallic copper as an antimicrobial surface," *Applied and environmental microbiology*, vol. 77, no. 5, pp. 1541–1547, 2011.